Microstructures and electrical properties of $Sr_{0.6}Bi_{0.4}Fe_{0.6}Sn_{0.4}O_3$–$BaCo^{II}_{0.02}Co^{III}_{0.04}Bi_{0.94}O_3$ thick-film thermistors with low room-temperature resistivity

Changlai Yuan · Tao Yang · Ying Luo · Changrong Zhou · Guohua Chen · Yun Yang

Abstract The thick film NTC thermistor of compositions $Sr_{0.6}Bi_{0.4}Fe_{0.6}Sn_{0.4}O_3$ + $BaCo^{II}_{0.02}Co^{III}_{0.04}Bi_{0.94}O_3$, synthesized by solid state reaction, were prepared by screen-printing on alumina substrate. The microstructures, composition dependent, impedance characteristics, self-heating behaviours and thermistor properties were investigated. The relation between logarithm of resistivity and reciprocal of absolute temperature for the thick film thermistor was almost linear for all the compositions studied. The room-temperature resistivity, thermistor constant and activation energy of the films decreased with increasing $BaCo^{II}_{0.02}Co^{III}_{0.04}Bi_{0.94}O_3$ content and were in the range of 18.2–945.7 Ω cm, 1,753–2,649 K and 0.151–0.228 eV, respectively. The thick films showed the nearest-neighbor hopping or variable-range hopping model depended on the compositions. Impedance analysis indicated that the resistivity value of the thick films was mainly ascribed to the contribution of grains. At higher $BaCo^{II}_{0.02}Co^{III}_{0.04}Bi_{0.94}O_3$ content, a good self-heating effect of one thermistor film was observed.

1 Introduction

Currently, negative temperature coefficient (NTC) thermistors are the most attractive temperature sensors due to the high temperature reliability and cost-efficiency. The NTC thermistor is a thermal sensitive resistor, in which the resistance shows a uniform exponential decrease with increasing temperature. Various bulk ceramics and thin/thick films with a wide range of adjustable thermistor parameters can be used in order to satisfy the market needs in the different industrial field and tune the device performance to the specific requirements [1–4]. In general, the bulk ceramics can easily achieve low room-temperature resistivity (ρ_{25}) and high thermistor constant (β) by tuning the compositions and dopants [5, 6]. For the thermistor thick/thin films, it is very difficult to obtain the low ρ_{25} and high β. Therefore, numerous studies have been conducted in order to improve NTC characteristics [7–9]. However, to date, these have not been successful in obtaining a high β constant with low room-temperature resistivity, because both are directly related to the size effect of grains and the extent of reaction/adhesion with the substrate. In order to solve one key problem of reducing ρ_{25} value of thermistor films, it is necessary to add some conductive phases into the film compositions [2, 10]. Simultaneously, another one is to seek a novel thermistor material with high β and modest room-temperature resistivity. By the combination of conductive phase and functional thermistor phase, it is reported that $LaNiO_3$–$NiMn_2O_4$ composite films with high β value of $\sim$5,000 K and modest room-temperature resistivity of $\sim$200 kΩ cm are successfully produced by Jungho Ryu et al. [11]. In previous studies, we also found a novel thermistor material of $Bi_{0.4}Sr_{0.6}Fe_{0.6}Sn_{0.4}O_3$ with high β and a new conductive phase of $BaCo^{II}_{0.02}Co^{III}_{0.04}Bi_{0.94}O_3$ with low ρ_{25} [12], respectively. A novel composite thick-film system is expected to obtain by using $BaCo^{II}_{0.02}Co^{III}_{0.04}Bi_{0.94}O_3$ phase as a semiconducting low resistive phase and $Bi_{0.4}Sr_{0.6}Fe_{0.6}Sn_{0.4}O_3$ as a high-resistance thermistor phase.

Next, we fabricate the $BaCo^{II}_{0.02}Co^{III}_{0.04}Bi_{0.94}O_3$–$Bi_{0.4}Sr_{0.6}Fe_{0.6}Sn_{0.4}O_3$ composite thick films by screen-printing technology. The microstructure, electrical

C. Yuan (✉) · T. Yang · C. Zhou · G. Chen · Y. Yang
School of Material Science and Engineering, Guilin University of Electronic Technology, Guilin 541004, People's Republic of China
e-mail: yclai-2002@163.com

Y. Luo
Guilin Academy of Air Force, Guilin 541004, People's Republic of China

Table 1 The values of ρ_{25}, $B_{25/85}$ and E_a for various thick films

Samples No.	Sintering temperatures (°C)	ρ_{25} (Ω cm)	$B_{25/85}$ (K)	E_a (eV)
BS50 ($x = 0.5$)	860	945.7	2,649	0.228
BS60 ($x = 0.6$)	840	215.3	2,458	0.212
BS70 ($x = 0.7$)	830	56.3	2,195	0.189
BS80 ($x = 0.8$)	820	18.2	1,753	0.151

properties and impedance characteristics of the novel thermistor film are closely investigated. Mixtures of the two phases are excellent for adjusting the thermistor parameters. Comparing with the conventional thermistor ceramics, the novel thick film NTC thermistors with low ρ_{25} and modest thermistor constant are more attractive from a system design, cost efficiency and manufacturing point of view.

2 Experimental details

$BaCo^{II}_{0.02}Co^{III}_{0.04}Bi_{0.94}O_3$ (abbreviated as BCCB) source powder was produced by mixing, grinding and firing the precursors $BaCO_3$, Bi_2O_3 and Co_3O_4. The mixtures were fired at 700 °C for 2 h. $Sr_{0.6}Bi_{0.4}Fe_{0.6}Sn_{0.4}O_3$ (abbreviated as SBFS) source powder was produced by firing the precursors $SrCO_3$, Bi_2O_3, Fe_2O_3 and SnO_2 for 4 h at 1,000 °C. Thermistor pastes (ink) were prepared by mixing the desired amounts of produced $BaCo^{II}_{0.02}Co^{III}_{0.04}Bi_{0.94}O_3$ and $Sr_{0.6}Bi_{0.4}Fe_{0.6}Sn_{0.4}O_3$ [$xBaCo^{II}_{0.02}Co^{III}_{0.04}Bi_{0.94}O_3$–$(1 - x)$ $Sr_{0.6}Bi_{0.4}Fe_{0.6}Sn_{0.4}O_3$, where x represents the molar ratios] source powders with the organic vehicle in order to obtain printable pastes (as shown in Table 1). Organic vehicle was a solution of ethyl cellulose, lecithin and 2-(2-butoxy ethoxy-ethyl) acetate. The inorganic to organic ratio was kept at 70:30 (w/w %). The resultant thick-film thermistor pastes were screen-printed onto a 96 % alumina substrate using a stainless screen of 250

mesh size, then settled down and dried under IR lamp for 10–15 min. This printing process was repeated ten times and the thickness of each printing was 5–8 μm. The printed patterns were fired in a muffle furnace at moderate temperatures with a dwell time of 60 min. All the organic components were decomposed after printing the films during the sintering process of thick films.

Samples were routinely characterized by X-ray diffraction (XRD) and scanning electron microscopy (SEM) equipped with energy disperse spectroscopy (EDS). The thickness of the fired films was 50–80 μm as measured by XP-100 high resolution stylus-type surface profilometer. The DC electrical resistance of thermistor films was measured using a digital multimeter (Fluke 45) from 25 to 200 °C with a step of 5 °C. The I–V characteristics of the BS80 thick film were measured by Keithley 2,400. For BS60 thick-film sample, impedance spectra were taken at temperatures 25–200 °C using an Agilent (4294A) Impedance Analyzer with computer controlled automated data collection, which increased the frequency logarithmically between 40 Hz and 5 MHz.

3 Results and discussion

XRD patterns of composite NTC thick films (Samples BS50–BS80) were shown in Fig. 1, where the numbers of BS50–BS80 represented the film compositions with different $BaCo^{II}_{0.02}Co^{III}_{0.04}Bi_{0.94}O_3$ content as shown in Table 1. From Fig. 1a, it is seen that the thick films are mainly composed of SBFS and BCCB phases. Some new phases such as $Sr_2Bi_2O_5$, $Bi_2Fe_4O_9$ and $BaBi_2O_{4+x}$, are observed besides the SBFS and BCCB phases. The occurrence of new phases is attributed to the chemical reaction and inter-diffusion of the phases between SBFS and BCCB source materials. The intensities of the diffraction peaks are an indicative of the percentages of the

Fig. 1 XRD patterns of screen-printed thick films at 2θ of **a** 20°–80°, **b** 28°–30° and **c** 40°–43°
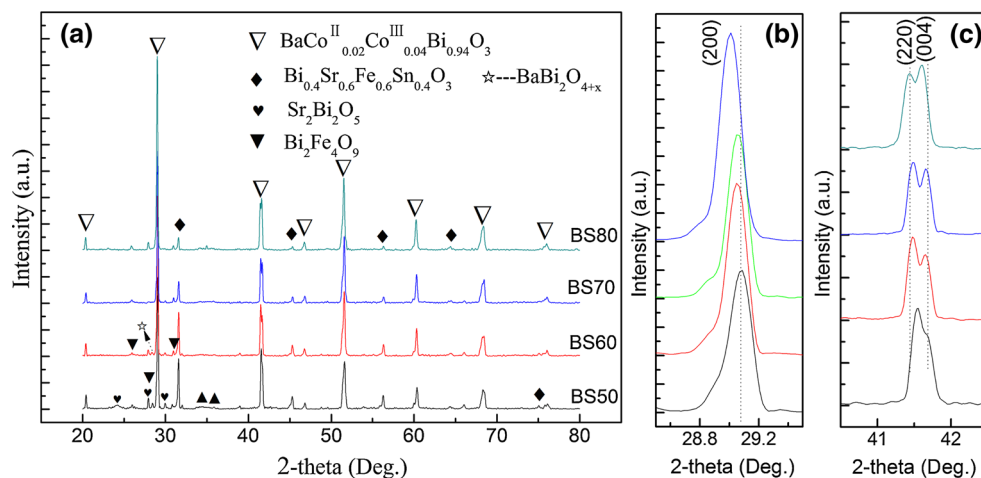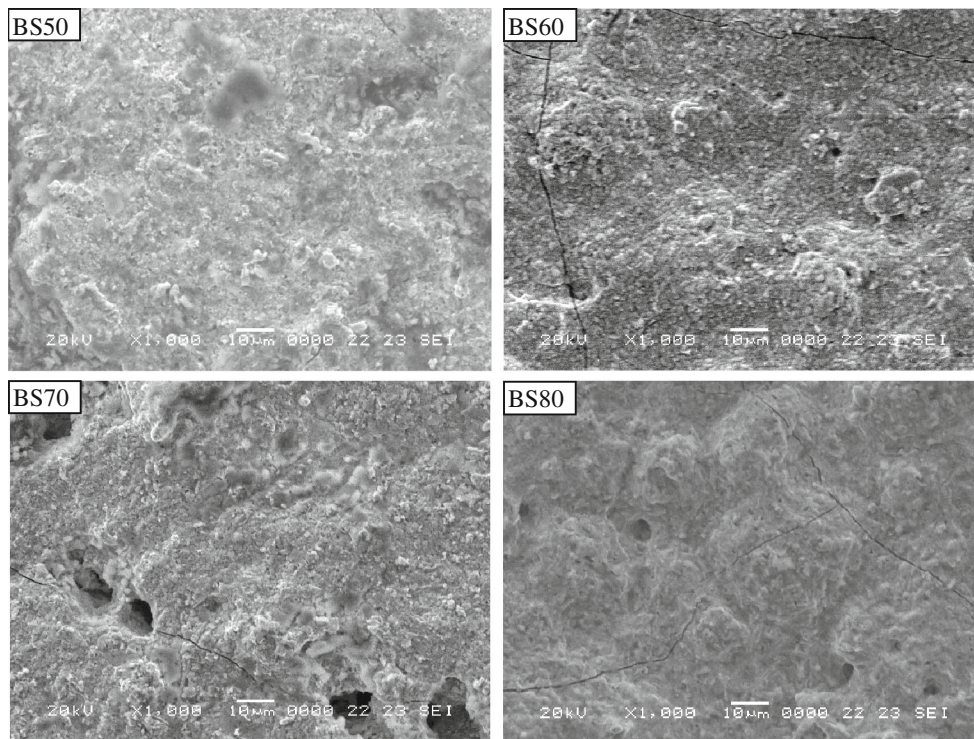
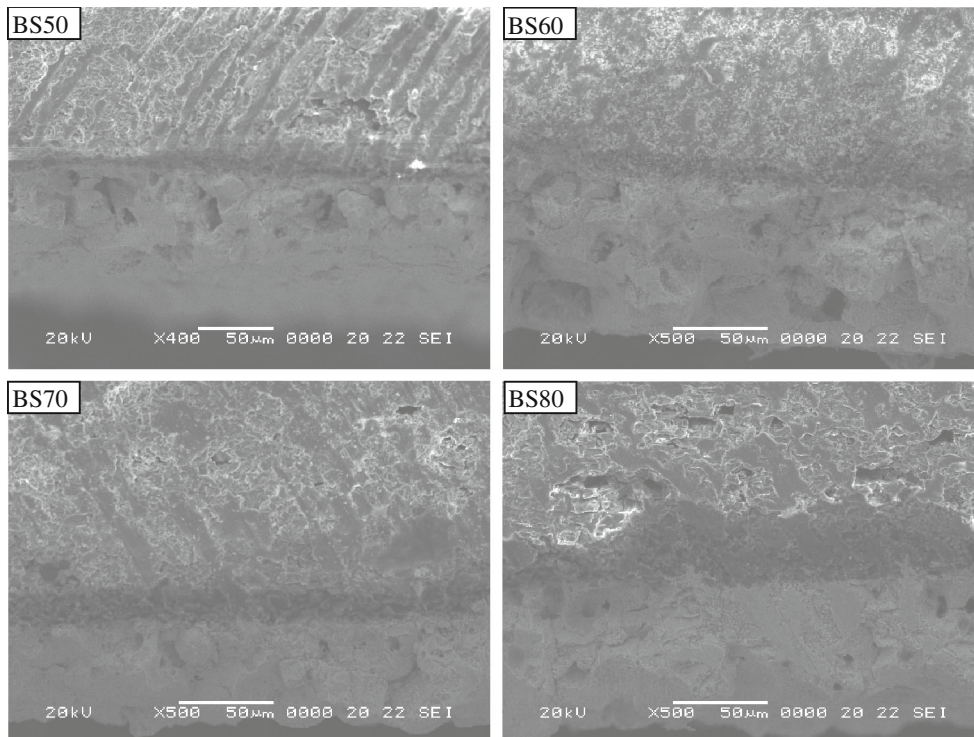**Fig. 2** SEM surface images of screen-printed thick films

Fig. 3 SEM cross-sectional images of screen-printed thick films

individual phases. With increasing content of BCCB (marked '▽') content, the peak intensity of the BCCB increased, which means that the film compositions followed the initial powder mixture compositions. Almost all highly conducting compounds with low melting point, including BCCB, are prone to decomposition at high
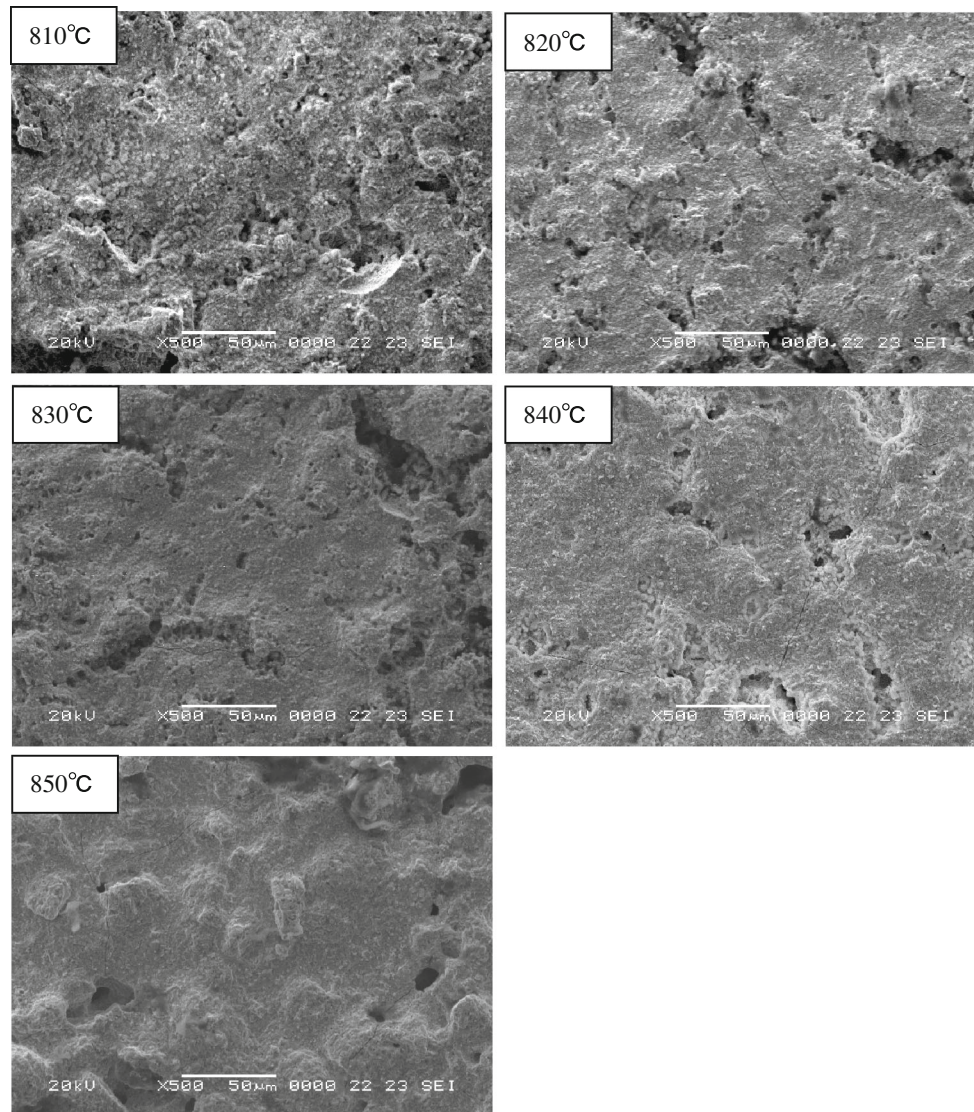
Fig. 4 SEM surface images of the BS60 thick films sintered at different temperatures

sintering temperature (>900 °C) [13, 14], thus no higher SBFS compositions are investigated in the composite films, in order to prevent any undesirable phase decomposition. From Fig. 1b and c, furthermore, it is found that the slight shift toward low diffraction angle was observed on the face (200) and a more obvious new diffraction peak occurred in the neighboring of the face (220). The shift to low angle denotes that some anions with small ionic radius entered into the B site of BCCB phase. It is believed that Fe^{3+} in SBFS phase was partly diffused into the BCCB phase and led to the low-angle shift due to a smaller ionic radius of Fe^{3+} than that of Bi^{3+} at the same coordination number. Simultaneously, it is observed that with increasing BCCB content, the peak intensity of crystal face (004) gradually became higher than that of face (220), which denotes that

the crystal growth orientation of the composite films shifted slowly to the (200) face from the (220) face.

Figures 2 and 3 show the surface and cross-sectional SEM micrographs of the thick films sintered at optimal temperature, respectively. The surface SEM micrographs show the typical surface microstructure of screen-printing films. The films are low-density and a little pore is observed in the surface micrographs of either film. From the cross-sectional micrographs of the films, the film thickness, which is controlled by the amount of repetitive printing cycles, is measured to be in the range of 50–80 μm. The thick films printed on the Al_2O_3 substrate show no peeling and adhere very well to the substrate. Generally, screen-printing films without glass additives require a relative high temperature sintering at over 900 °C

Fig. 5 SEM cross-sectional images of thick-film sample BS50 with **a** low magnification and **b** high magnification; EDS spectra of **c** spot '1' and **d** spot '2' in Fig. 5b
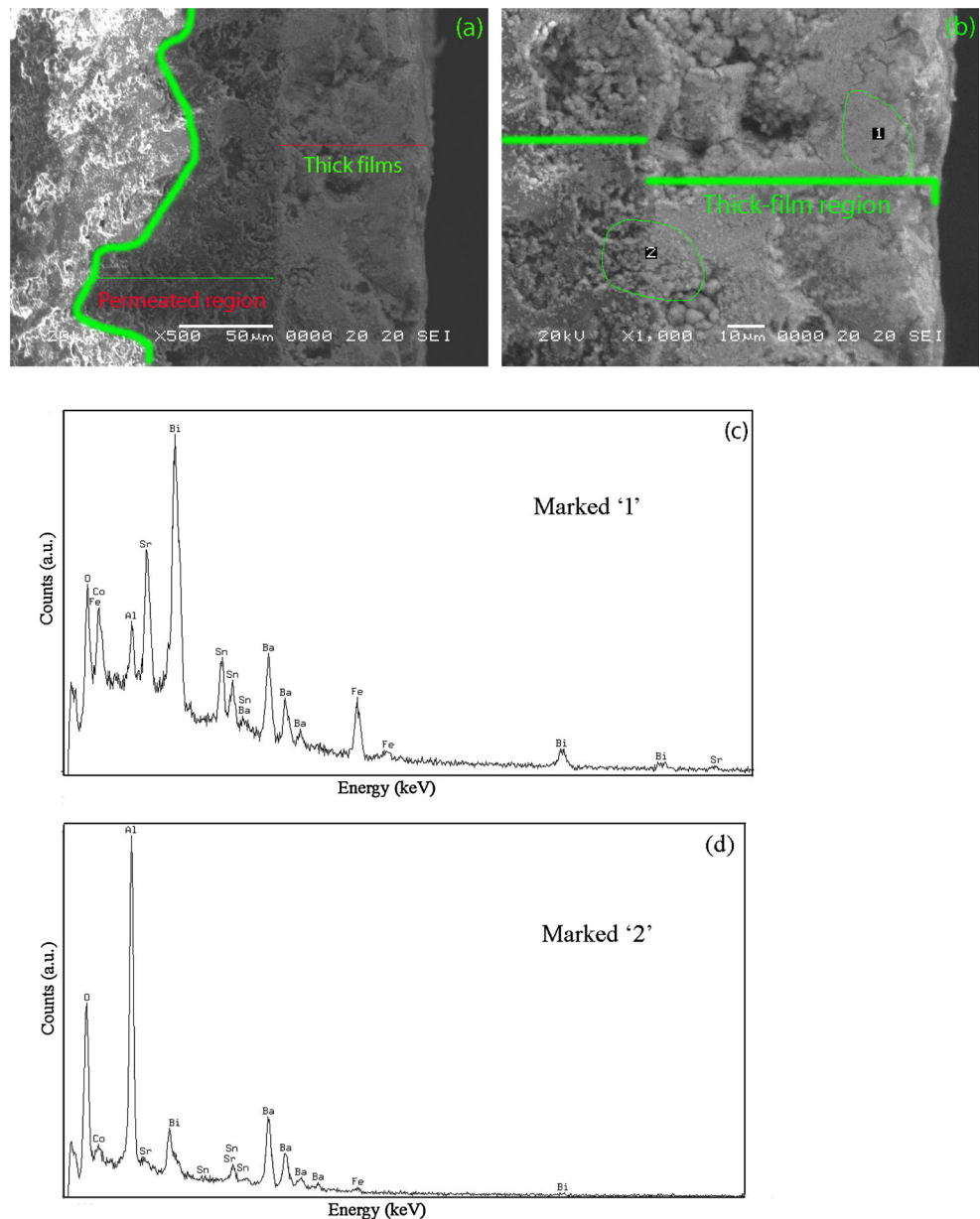
[7, 15]. However, the sintered temperatures of current NTC thick films are not as high as the films without glass frits, which indicate that the BCCB phase acted as the same role as the glass additive in thick-film preparation. From Fig. 2, it is also observed that the compactness of the films was obviously improved with the increasing BCCB content. This confirms further the importance of BCCB phase during the sintering processes of the composite films. Figure 4 shows the SEM images obtained from the surface of the BS60 sample sintered at 810–850 °C. The sintered bodies are porous compared to the bulk samples. This is due to the low pressure during the screen printing and the evolution of organic binders during the sintering processes. As expected, the compactness of the sintered bodies increases with increasing sintering temperature.

In order to obtain the interface compositions between the thick film and Al_2O_3 substrate, the BS50 sample sintered at 860 °C was selected to have the EDS measurement and the obtained SEM image was shown in Fig. 5a. In this figure, it is found that the composite film was partly permeated into the substrate and a wide-range permeating region was clearly observed in the figure. By the further magnification of the figure as shown in Fig. 5b, two regions marked '1' and '2' in Fig. 5b were zoomed to have the EDS measurement and the results were shown in Fig. 5c–d. Region '2' which represents the film–substrate contact interface, is mainly made of element Al and small amount of Bi, Ba and O. Region '1' contains the key elements Bi, Ba, Fe, Sn, Sr, O and Al, which means that the region was still composed of BCCB and SBFS phases. Based on the

element analysis, it can be confirmed that the composition inter-diffusion of film-substrate contacting interface was very strong and helped to maintain good adhesion with substrate.

Figure 6a shows a plot of $\log \rho$ versus the reciprocal absolute temperature of either film. The *log* resistivity of all the films decreases linearly with increasing absolute temperature, which confirms that the films followed Nernst–Einstein relation [16]. The room-temperature resistivity (ρ_{25}), thermistor constant ($\beta_{25/85}$), and activation energy (E_a) are the most important characteristic parameters of NTC thermistors, and are summarized in Table 1. The calculated values of ρ_{25}, $\beta_{25/85}$ constant, and E_a of the composite NTC thermistor films are in the range 18.2–945.7 Ω cm, 1,753–2,649 K, and 0.151–0.228 eV, respectively. The addition of BCCB yields a decrease in the ρ_{25} and the $\beta_{25/85}$ constant. This is due to that at a relatively low loading level of BCCB conductive particles, the conductive BCCB particles are widely separated by high-resistive SBFS particles and the SBFS particles acts as a barrier to the follow of mobility carriers from BCCB phase, resulting into a higher level of electrical-resistivity value. Thereafter, with the increase of BCCB conductive particles, the conductive particle aggregates get more tightly packed and the gap distance between them becomes smaller, which denotes that the barrier between conductive particles decreased and thus helps to reduce the electrical resistivity. This means that there are two conduction mechanisms coexisting in the composite films, where one is the small polaron hopping model and another one is the chain mechanism [17, 18].

The relationship between the logarithmic electrical resistivity and the reciprocal of the absolute temperature (1/T) for the BS60 sample sintered at 810–850 °C was obtained, as shown in Fig. 6b. This figure reveals that the thermistors operated steadily with the linear dependence between the two parameters over a wide temperature range. The room-temperature resistivity of the as-sintered films is firstly 444.7 Ω cm and then it decreases to the lowest value of 215.3 Ω cm as the sintered temperature is increased up to 840 °C (as shown in Table 2). These can be elucidated by chain mechanism that the compactness of thermistor films is weak when the sintering temperature is low and the film density increases with the rise of heat-treatment temperature. The compactness or density enhancement helps to reduce the gap distance between conductive particles and effectively improve the electrical conductivity of thermistor films. However, the BS60 sample sintered at 850 °C shows a slight abnormal increase of ρ_{25}. The abnormality may be caused by Al_2O_3 from the substrate. From Fig. 5c, it is well known that the Al_2O_3 from the substrate was partly permeated into the thick films. As the film is over-heated during the sintering processes, the more Al_2O_3 is entered into the thick films and urges the ρ_{25} value to
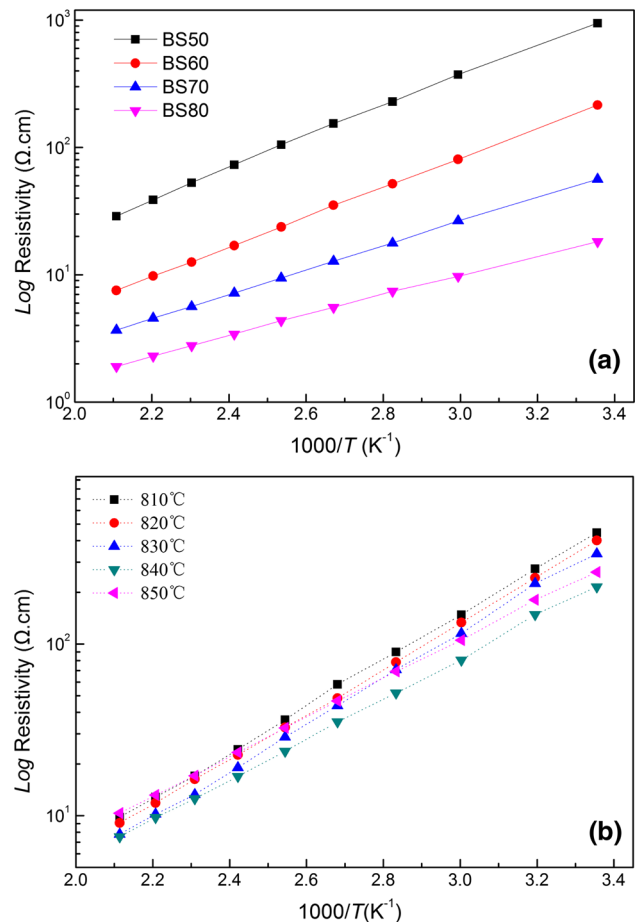

Fig. 6 Relationship between $\log\rho$ and the reciprocal of absolute temperature **a** for the SBFS−BCCB composite NTC thick films and **b** for the BS60 sample sintered at 810–850 °C

Table 2 The values of ρ_{25}, $B_{25/85}$ and E_a for the BS60 samples sintered at different temperatures

Sintering T (°C)	ρ_{25} (Ω cm)	$B_{25/85}$ (K)	E_a (eV)
810	444.7	3,125	0.270
820	404.7	3,121	0.269
830	335.2	2,997	0.258
840	215.3	2,458	0.212
850	261.9	2,558	0.221

increase. Thus, it is believed that for the B60 sample sintered at 850 °C, the over-heating behavior arose and led to the abnormal resistivity increase. The activation energies of the films sintered at 810, 820, 830, 840 and 850 °C are 0.270, 0.269, 0.258, 0.212, and 0.221 eV, respectively. The reasons of the reduction in β constant and activation energy for non over-heatment films are difficult to explain but are presumably related to the grain growth with high crystallinity and the reduced area of grain boundaries.
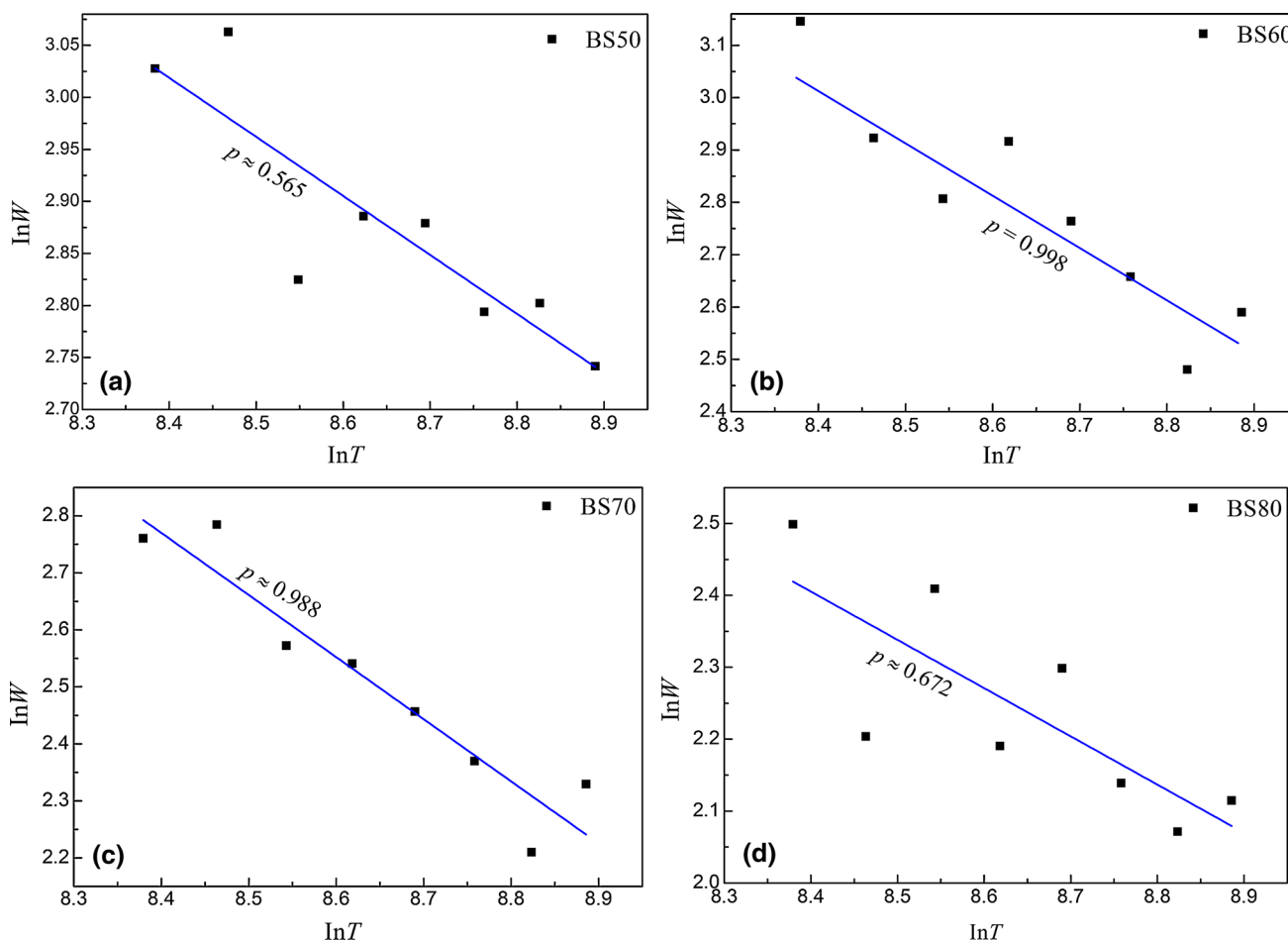
Fig. 7 ln(W) versus ln(T) *plots* for SBFS − BCCB composite NTC thick films

It is well known that the dc R–T curves in polycrystalline NTC materials had followed the small-polaron hopping model in nonadiabatic regime for nearest-neighbor- or variable-range hopping (NNH, VRH) [17]. Both types of hopping can be described by a general expression [19, 20].

$$R(T) = CT^{\alpha} \exp(T_0/T)^p \qquad (1)$$

where C is the temperature independent contribution to the R, T is the absolute temperature, T_0 is a characteristic temperature and p is the exponential power law. For conventional VRH $0.25 < p = \alpha/2 < 1$ while for NNH $\alpha = p = 1$. p is the negative slope of a plot ln(W) VS lnT, where W is defined as [17].

$$W = \frac{1}{T} \frac{d(lnR)}{d(T^{-1})} \approx -p\left(\frac{T_0}{T}\right)^P \qquad (2)$$

This is a powerful technique to elucidate the character of hopping motion in semiconducting materials. In current studies, the calculated p values based on the R–T curves of Fig. 6a are shown in Fig. 7. Obviously, the conduction mechanism of samples BS60 and BS70 can be well

described by NNH, whereas that of samples BS50 and B80 can be described by VRH. Considering that the p values of samples BS50 and B80 (0.565, 0.672) is a rather low exponent for conventional VRH, here we suggest that the hopping type of the two samples should be further thought as Efros–Shklovskii VRH [17, 21].

The ac impedances of the BS60 sample at 25–200 °C are plotted as Cole–Cole spectra. To assess the shape and overlapping of each electrical component, the data of ac impedances on linear scale are shown in Fig. 8. Single suppressed semicircles at 25°Cindicate that the grain-boundary ($CPE_{gb}R_{gb}$) and grain (CPE_gR_g) semicircles have a strong overlap in the thick film. Simultaneously, a very small arc attributed to an electrode effect (CPE_eR_e) is observed in Fig. 8a. By fitting the impedance data using the commercial software of Z-View2 and the equivalent circuit models in Fig. 8e–f, the average electrical resistances of the grains and grain boundaries are 3.63×10^5 and $3.77 \times 10^4 \, \Omega$, respectively. As the measured temperatures are equal to or above 40 °C, only a single semicircle in Fig. 8b–d is observed and the contributions from the grain
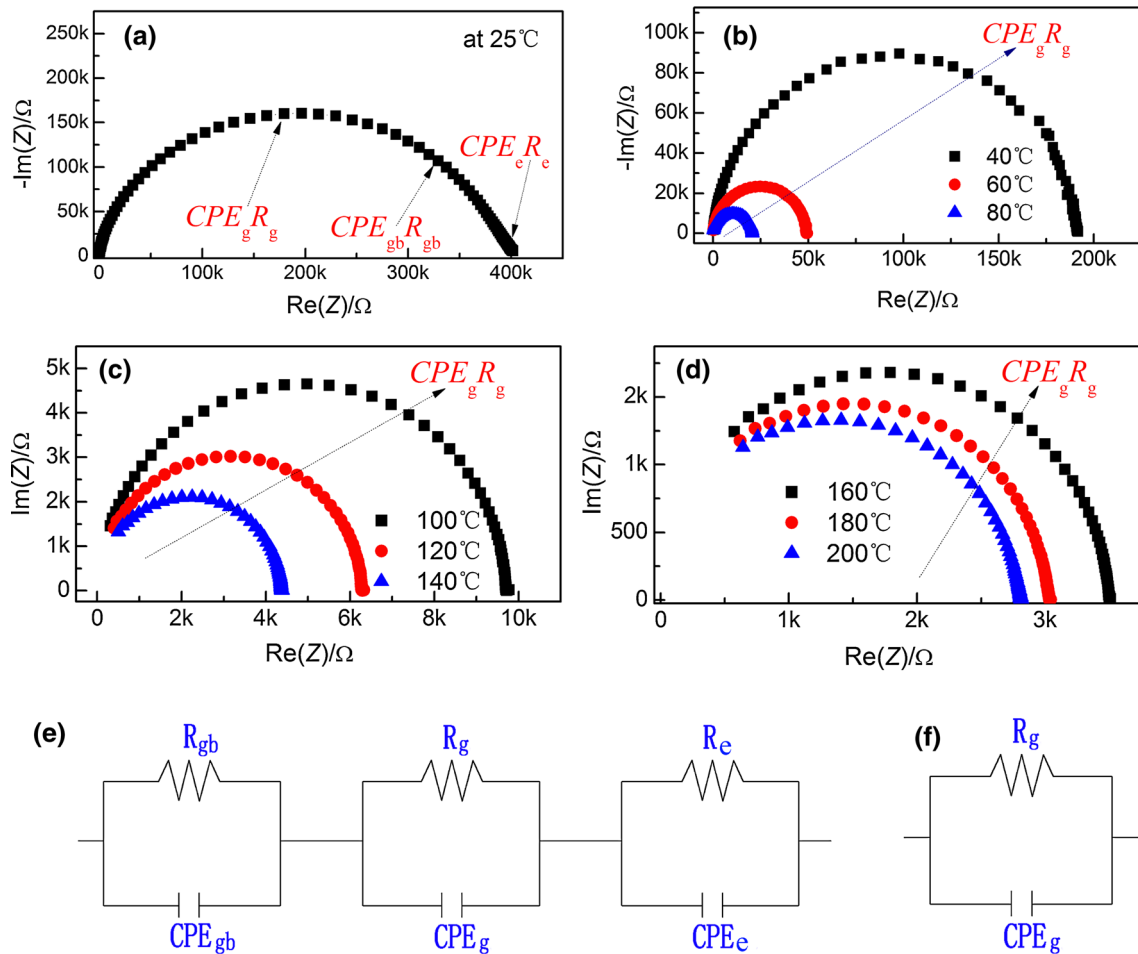
Fig. 8 AC impedance spectroscopy of the BS60 thick film measured at **a** 25 °C, **b** 40–80 °C, **c** 100–140 °C and **d** 160–200 °C on a linear scale; The equivalent circuit models in **e** and **f** are used for fitting the impedance data in Fig. 8a and in Fig. 8b–d, respectively

boundaries or electrodes are surprisingly vanished or negligible. The only semicircle is believed to be identified as the grain response due to the low capacitance value of $\sim 3.0 \times 10^{-11}$ F. Obviously, the resistance value of grain boundaries at 25 °C is one order of magnitude lower than that of grains and is too small to be extracted at higher measured temperatures, which is abnormality compared to the conventional bulk ceramics. It is deduced that the mixture of BCCB and SBFS phases formed the single particle similar to core–shell structure, where the BCCB phase is in the shell layer due to low melting point and the SBFS in the core layer. The formation of core–shell structure denotes that the micro-region composition in the contact interfaces amongst the particles or grain boundaries is mainly composed of the BCCB phase. Thus, this makes the resistance value of grain boundaries made of conductive BCCB phase is lower that that of grains. However, the deduction is still to be the further investigation.

One of the most interesting and useful property of an NTC thermistor is the self-heating behaviour [22]. Figure 9

shows the typical *I–V* curve or self-heating process of the BS80 film at room temperature after sufficient time has been kept over the film for achieving a steady state. At low currents, the power dissipated in the thermistor is too low to heat the thermistor. In the current region, the low current through the film is not sufficient to raise the temperature of the device and the *I–V* behavior obeys the ohmic law. Thereafter, an increase in current causes a reduction in thermistor resistance. This decrease in resistance is due to heating development in the thermistor itself by the action of current through it. A peak value of voltage ($U_{max} = 45.0$ V) occurs at a current of 31.8 mA where the thermistor-body temperature rises. With further increase up to 120.0 mA in the current, self heating effect is caused so much that the resulting drop in voltage induces a fall in resistance. The falling region in voltage exhibits a negative resistance with rise of current and a steady state is gradually reached where thermistor dissipates as much power as is supplied to it. However, with further increase in the current to much higher than 120 mA, thermistor film might
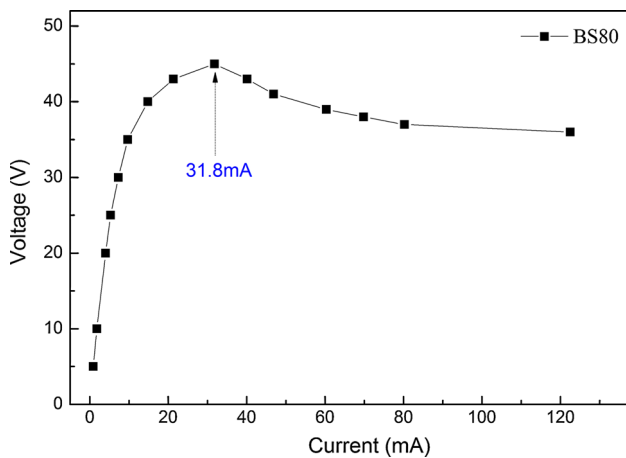
Fig. 9 Current–voltage (*I–V*) characteristics of the BS80 thick film at room temperature

could be used as potential candidates for NTC thermistors in the field with low room-temperature resistivity.

cause the thermal mismatch between the thermistor and the substrate which presumably damages the alumina substrate as well as the thermistor film. Similar I–V characteristics are also observed in Ref. [23].

4 Conclusions

The $BaCo^{II}_{0.02}Co^{III}_{0.04}Bi_{0.94}O_3$–$Bi_{0.4}Sr_{0.6}Fe_{0.6}Sn_{0.4}O_3$ composite thick films were prepared by screen-printing technique. XRD patterns indicated that the phases of composite films were mainly composed of $BaCo^{II}_{0.02}Co^{III}_{0.04}Bi_{0.94}O_3$ and $Bi_{0.4}Sr_{0.6}Fe_{0.6}Sn_{0.4}O_3$ phases and some new phases such as $Sr_2Bi_2O_5$, $Bi_2Fe_4O_9$ and $BaBi_2O_{4+x}$ were observed. The Fe^{3+} in $Bi_{0.4}Sr_{0.6}Fe_{0.6}Sn_{0.4}O_3$ phase was found to enter into the lattices of $BaCo^{II}_{0.02}Co^{III}_{0.04}Bi_{0.94}O_3$ phase and then induced the low-angle shift of diffraction peaks due to the smaller ionic radius of Fe^{3+} than that of Bi^{3+}. The crystal growth orientation of the composite films shifted slowly to the (200) face from the (220) face with increasing $BaCo^{II}_{0.02}Co^{III}_{0.04}Bi_{0.94}O_3$ content. The calculated values of ρ_{25}, $\beta_{25/85}$ constant, and E_a of the composite NTC thermistor films are in the range 18.2–945.7 Ω cm, 1,753–2,649 K, and 0.151–0.228 eV, respectively. The addition of $BaCo^{II}_{0.02}Co^{III}_{0.04}Bi_{0.94}O_3$ led to a decrease in the ρ_{25} and the $\beta_{25/85}$ constant. The conduction mechanism of the samples containing 60 and 70 mol. % $BaCo^{II}_{0.02}Co^{III}_{0.04}Bi_{0.94}O_3$ phase can be well described by NNH model, whereas that of samples containing 50 and 80 mol. % $BaCo^{II}_{0.02}Co^{III}_{0.04}Bi_{0.94}O_3$ phase can be elucidated by VRH model. The total resistance of thick film is mainly attributed to the contribution of grains instead of conventional grain boundaries by the impedance analysis. Thermistor film of BS80 shows a good self-heating behaviour at room temperature, a characteristic with a peak value of voltage ($U_{max} = 45.0$ V) at a current of 31.8 mA. The films

References

1. M. Vakiv, O. Shpotyuk, O. Mrooz, I. Hadzaman, Controlled thermistor effect in the system $Cu_xNi_{1-x-y}Co_{2y}Mn_{2-y}O_4$. J. Eur. Ceram. Soc. **21**, 1783–1785 (2001)
2. S. Jagtap, S. Rane, S. Gosavi, D. Amalnerkar, 'Lead Free' thick film thermistors: a study of variation in glass frit concentration and organics composition. J. Mater. Sci.: Mater. Electron. **21**, 861–867 (2010)
3. M. Parlak, T. Hashemi, M.J. Hogan, A.W. Brinkman, Electron beam evaporation of nickel manganite thin-film negative temperature coefficient thermistors. J. Mater. Sci. Lett. **17**, 1995–1997 (1998)
4. C.L. Yuan, X.Y. Liu, M.F. Liang, C.R. Zhou, H. Wang, Electrical properties of Sr–Bi–Mn–Fe–O thick-film NTC thermistors prepared by screen printing. Sens. Actuators A **167**, 291–296 (2011)
5. C.H. Zhao, B.Y. Wang, P.H. Yang, L. Winnubst, C.S. Chen, Effects of Cu and Zn co-doping on the electrical properties of $Ni_{0.5}Mn_{2.5}O_4$ NTC ceramics. J. Eur. Ceram. Soc. **28**, 35–40 (2008)
6. K. Park, J.K. Lee, Mn–Ni–Co–Cu–Zn–O NTC thermistors with high thermal stability for low resistance applications. Scr. Mater. **57**, 329–332 (2007)
7. S.A. Kanade, V. Puri, Composition dependent resistivity of thick film $Ni_{(1-x)}Co_xMn_2O_4$: ($0 \leq x \leq 1$) NTC thermistors. Mater. Lett. **60**, 1428–1431 (2006)
8. S.A. Kanade, V. Puri, Electrical properties of thick-film NTC thermistor composed of $Ni_{0.8}Co_{0.2}Mn_2O_4$ ceramic: effect of inorganic oxide binder. Mater. Res. Bull. **43**, 819–824 (2008)
9. R. Schmidt, A. Basu, A.W. Brinkman, Production of NTCR thermistor devices based on $NiMn_2O_{4+\sigma}$. J. Eur. Ceram. Soc. **24**, 1233–1236 (2004)
10. S. Jagtap, S. Rane, R. Aiyer, S. Gosavi, D. Amalnerkar, Study of microstructure, impedance and dc electrical properties of RuO_2–spinel based screen printed 'green' NTC thermistor. Curr. Appl. Phys. **10**, 1156–1163 (2010)
11. J.-E. Kang, J. Ryu, G.F. Han, J.-J. Choi, W.-H. Yoon, B.-D. Hahn, J.-W. Kim, C.-W. Ahn, J.H. Choi, D.-S. Park, $LaNiO_3$ conducting particle dispersed $NiMn_2O_4$ nanocomposite NTC thermistor thick films by aerosol deposition. J. Alloys Compd. **534**, 70–73 (2012)
12. C.L. Yuan, X.Y. Liu, C.R. Zhou, J.W. Xu, B. Li, Electrical properties of lead-free thick film NTC thermistors based on perovskite-type $BaCo^{II}_xCo^{III}_{2x}Bi_{1-3x}O_3$. Mater. Lett. **65**, 836–839 (2011)
13. J.-J. Choi, J. Ryu, B.-D. Hahn, W.-H. Yoon, B.-K. Lee, J.-H. Choi, D.-S. Park, Ni-containing conducting ceramic as an oxidation protective coating on metallic interconnects by aerosol deposition. J. Am. Ceram. Soc. **93**, 1614–1618 (2010)
14. G.F. Han, J. Ryu, W.-H. Yoon, J.-J. Choi, B.-D. Hahn, J.-W. Kim, D.-S. Park, Effect of electrode and substrate on the fatigue behavior of PZT thick films fabricated by aerosol deposition. Ceram. Int. **38**, S241–S244 (2012)
15. K. Park, D.Y. Bang, Electrical properties of Ni–Mn–Co–(Fe) oxide thick-film NTC thermistors prepared by screen printing. J. Mater. Sci.: Mater. Electron. **14**, 81–87 (2003)
16. E.D. Macklen, *Thermistor* (Electrochemical Publications Ltd., Ayr, Scotland, 1979), p. 33

17. R. Schmidt, A. Basu, A.W. Brinkman, Small polaron hopping in spinel manganates. Phys. Rev. B **72**, 115101 (2005)
18. F. El-Tantawy, New double negative and positive temperature coefficients of conductive EPDM rubber TiC ceramic composites. Eur. Polym. J. **38**, 567–577 (2002)
19. R. Schmidt, A. Basu, A.W. Brinkman, Z. Klusek, P.K. Datta, Electron-hopping modes in $NiMn_2O_{4+\delta}$ materials. Appl. Phys. Lett. **86**, 073501 (2005)
20. R. Schmidt, A.W. Brinkman, Studies of the temperature and frequency dependent impedance of an electroceramic functional oxide NTC thermistor. Adv. Funct. Mater. **17**, 3170–3174 (2007)
21. B.I. Shklovskii, A.L. Efros, in *Electronic Properties of Doped Semiconductors, Solid State Sciences 45*, ed. by M. Cardona, P. Fulde, H.J. Queisser (Springer, Berlin, 1984)
22. A.U. Keskin, A simple analog behavioural model for NTC thermistors including selfheating effect. Sens. Actuators A **118**, 244–247 (2005)
23. S. Jagtap, S. Rane, S. Gosavi, D. Amalnerkar, Study on I–V characteristics of lead free NTC thick film thermistor for self-heating application. Microelectron. Eng. **88**, 82–86 (2011)